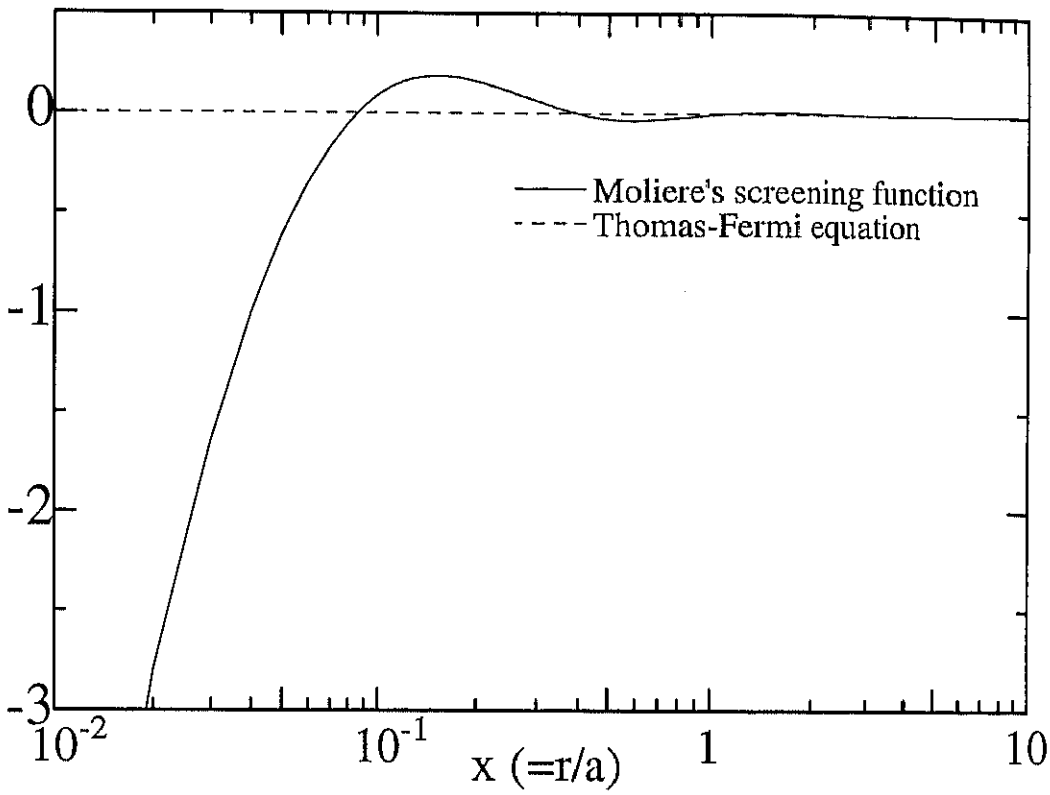

Figure 21: The result of inserting the Molière potential into Thomas-Fermi equation Eqn.48:

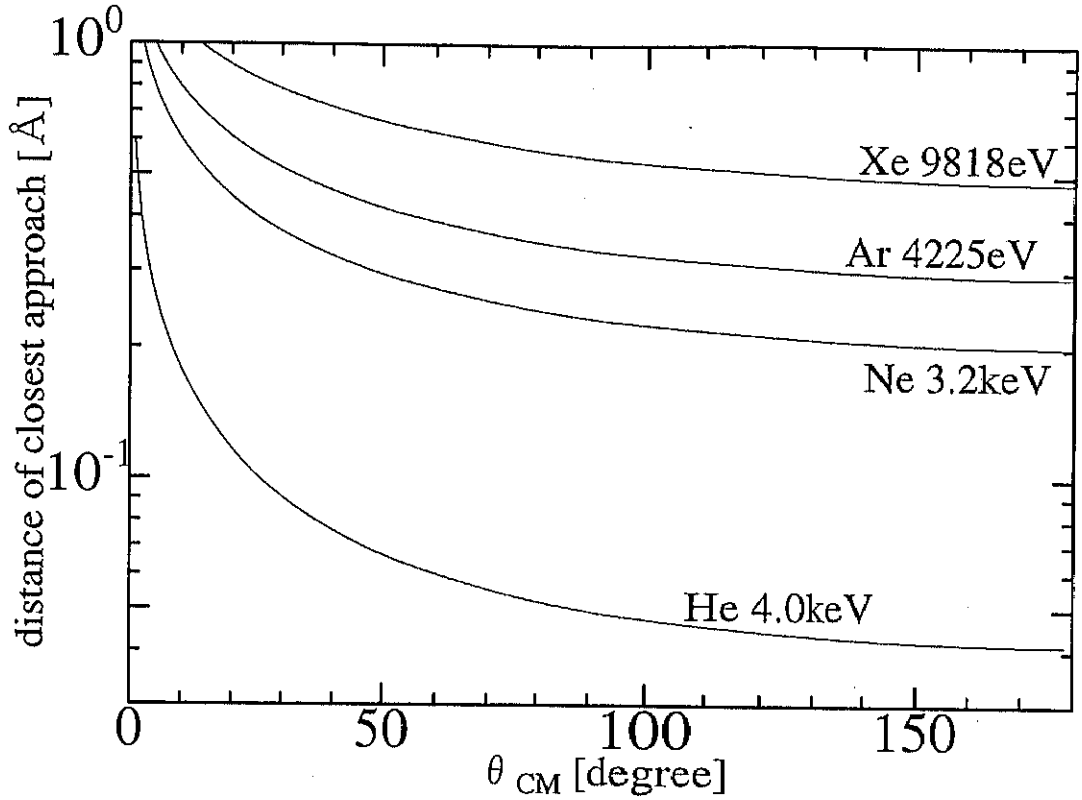

Figure 22: The distance of closest approach deduced by Molière potential function:

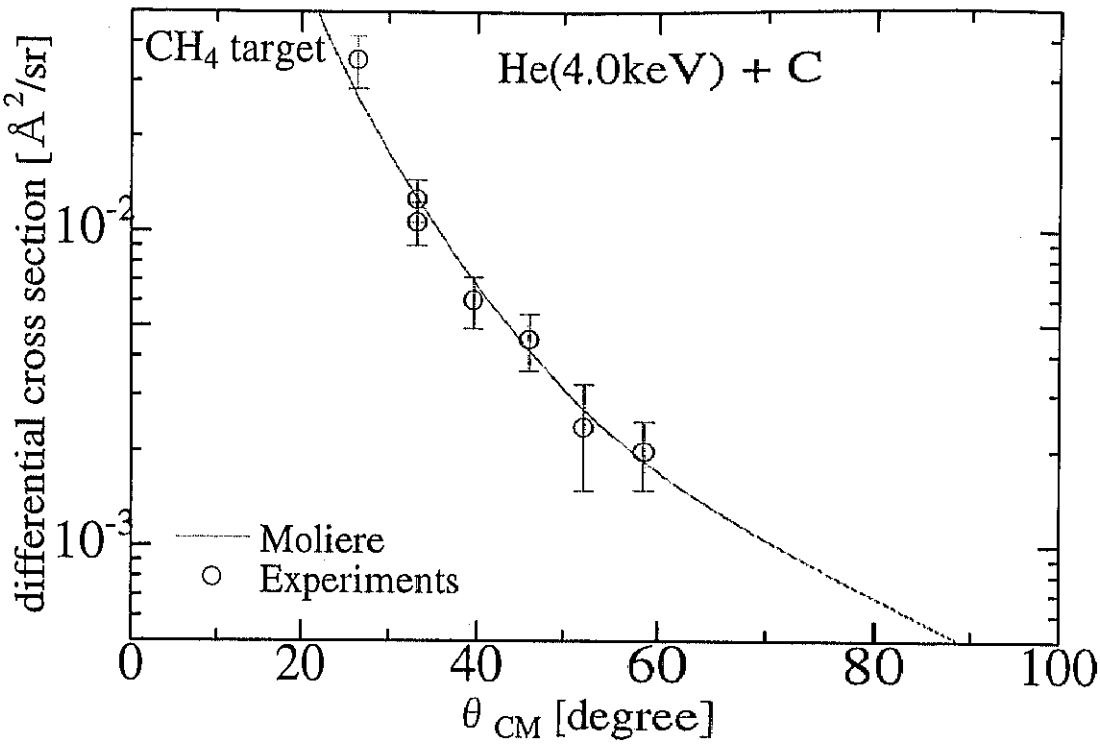

Figure 23: The angular distribution of scattered He with C in CH_4 target: The angular distribution is well fitting to the binary collision calculation using Molière potential.

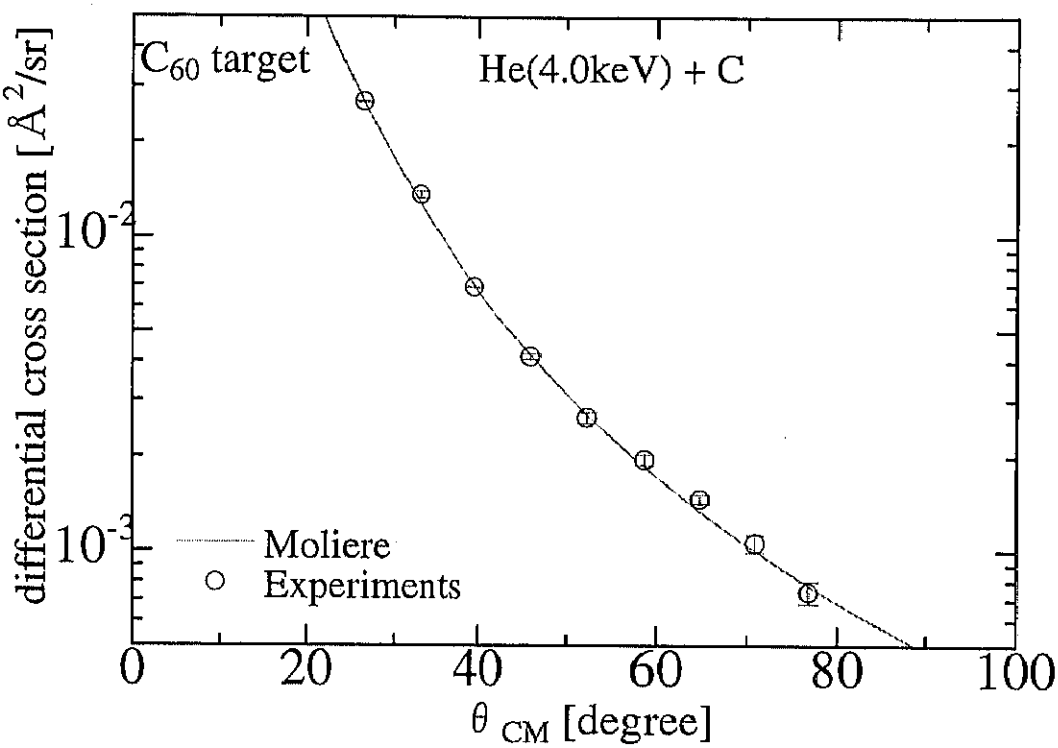

Figure 24: The angular distribution of scattered He with C in C_{60} target: The angular distribution is also perfectly fitting to the binary calculation. Therefore we use this result to deduce the absolute values of differential cross section by normalizing.

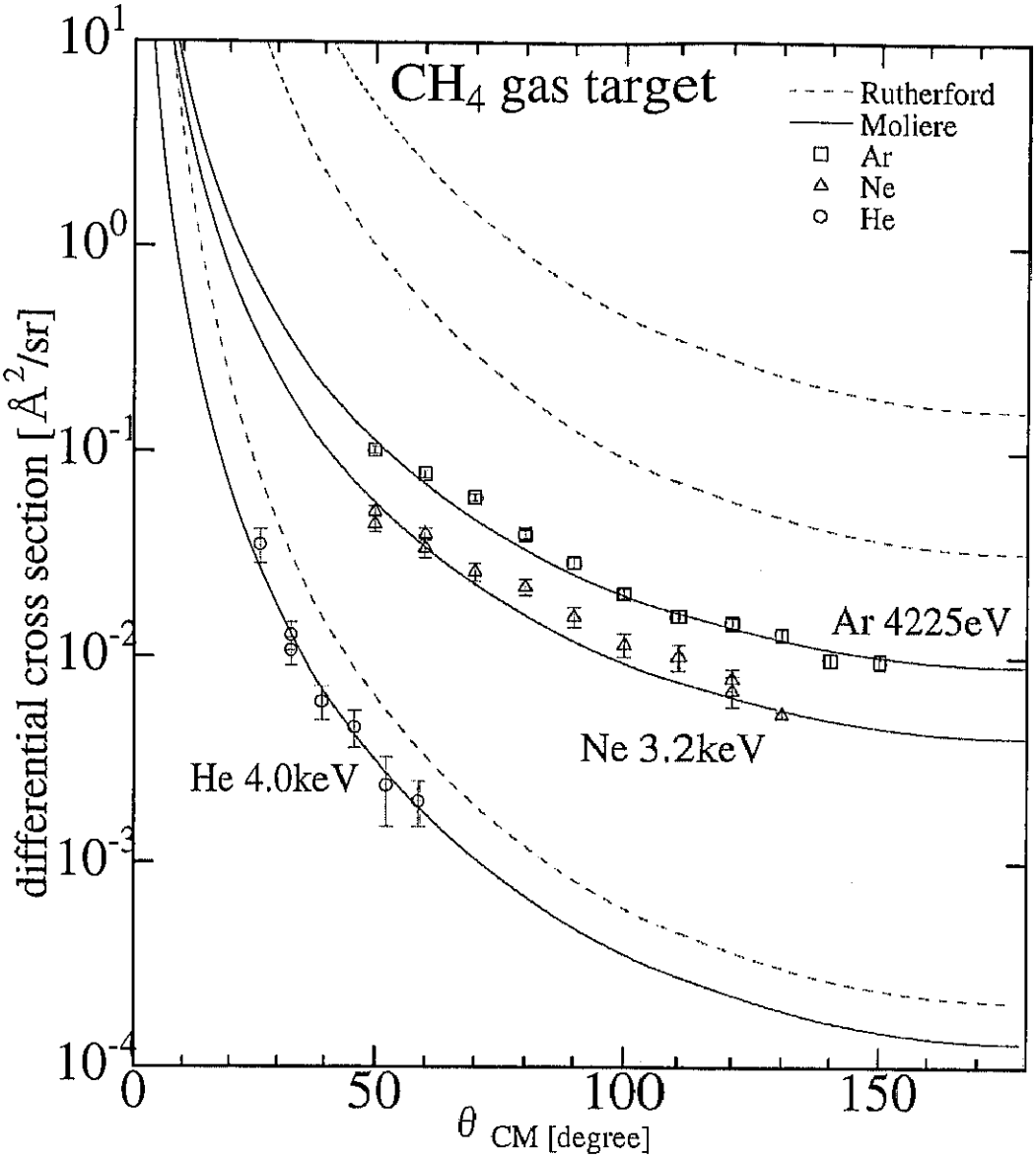

Figure 25: The differential cross sections of collision noble gas atoms with carbon in CH_4 target: The dashed lines indicate the calculation without screening effect (i.e. Coulomb force only). The electronic screening effect succeeds to describe the experimental data completely in the case of CH_4 target.

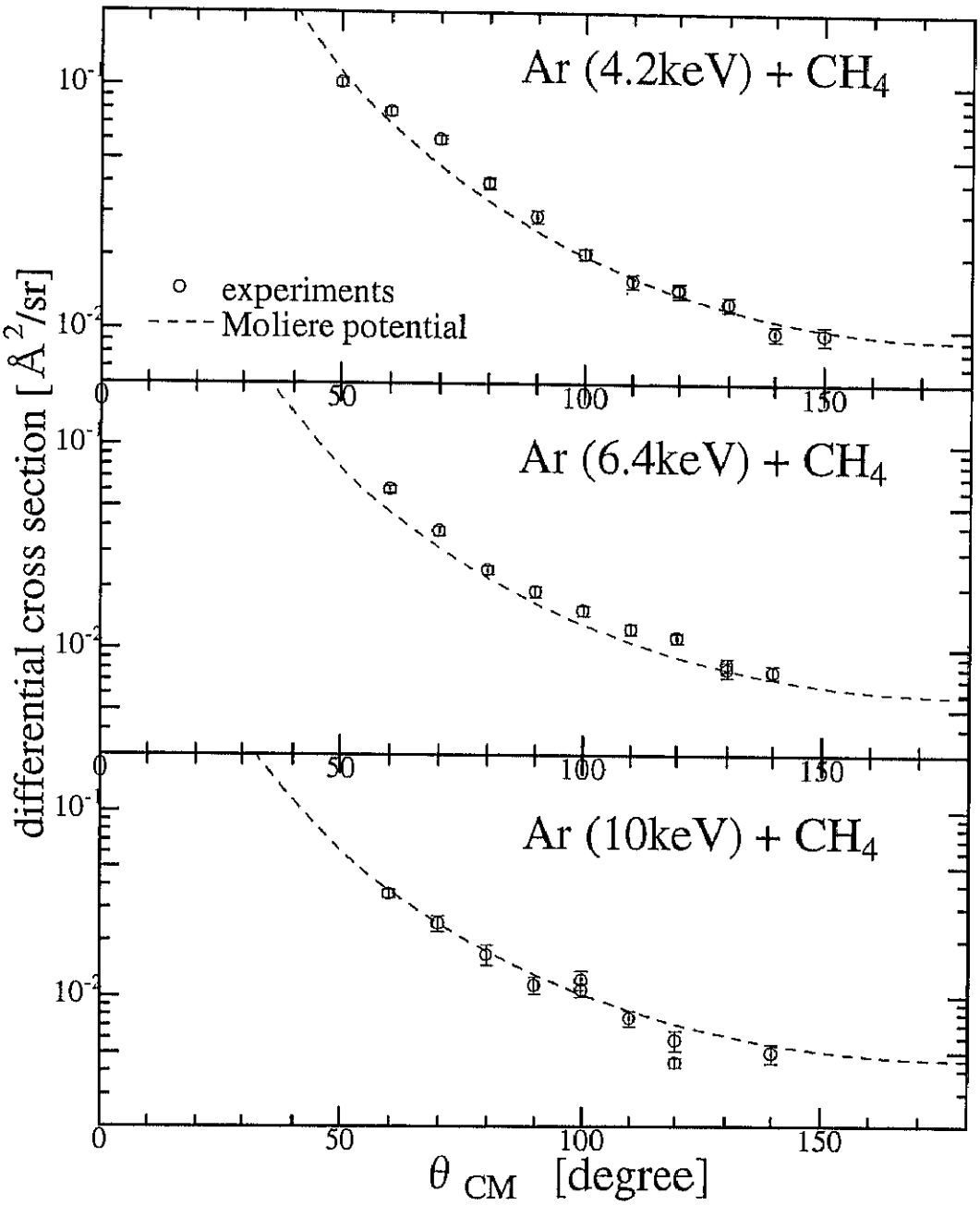

Figure 26: The differential cross sections of collision argon atom with carbon in CH_4 target at 4225eV to 10keV: The measurements are well accounted for the theoretical calculations for each energy.

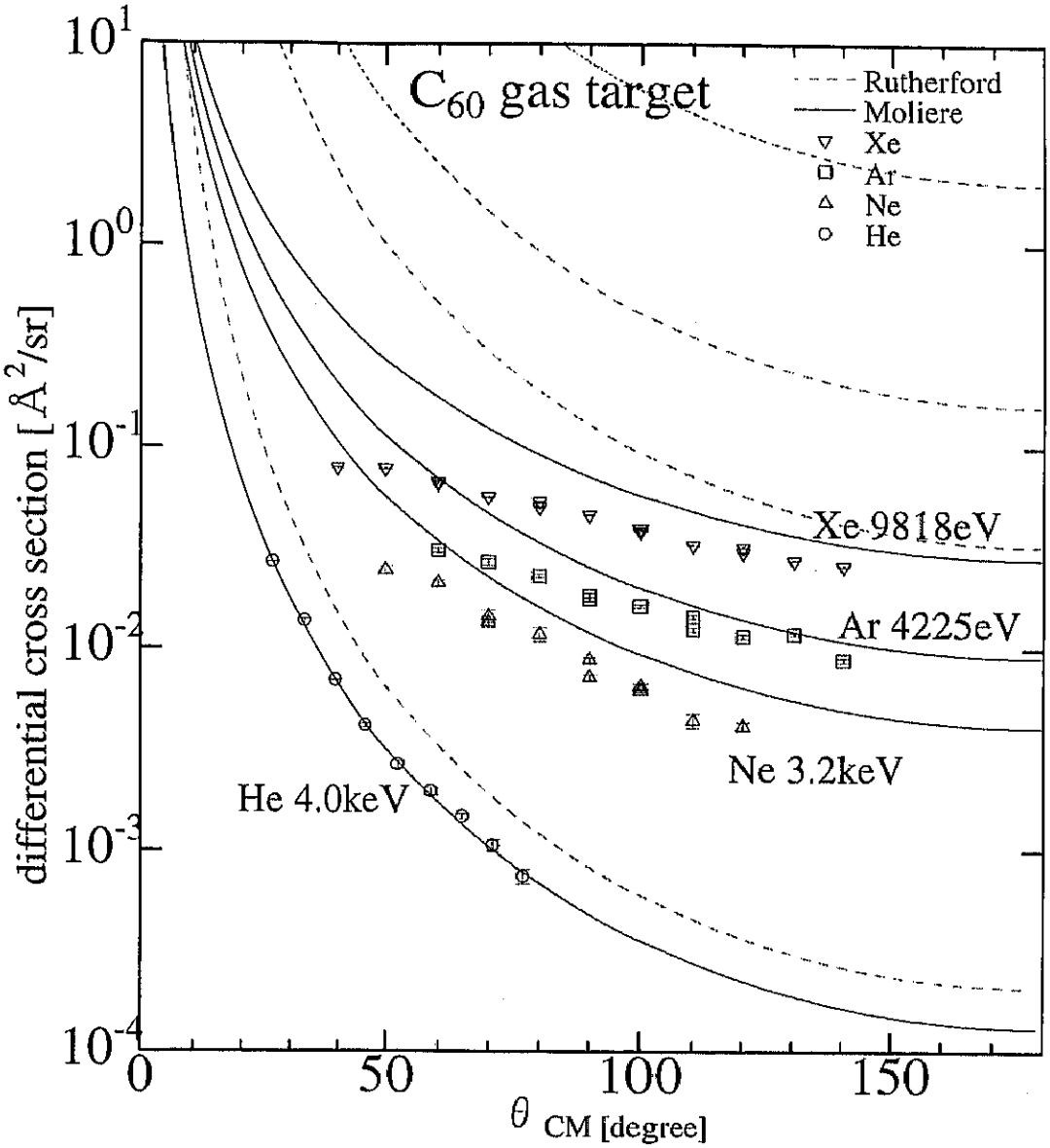

Figure 27: The differential cross sections of collision noble gas atoms with carbon in C_{60} target: Some systematic discrepancies are shown in the case of C_{60} target, especially at forward angles.

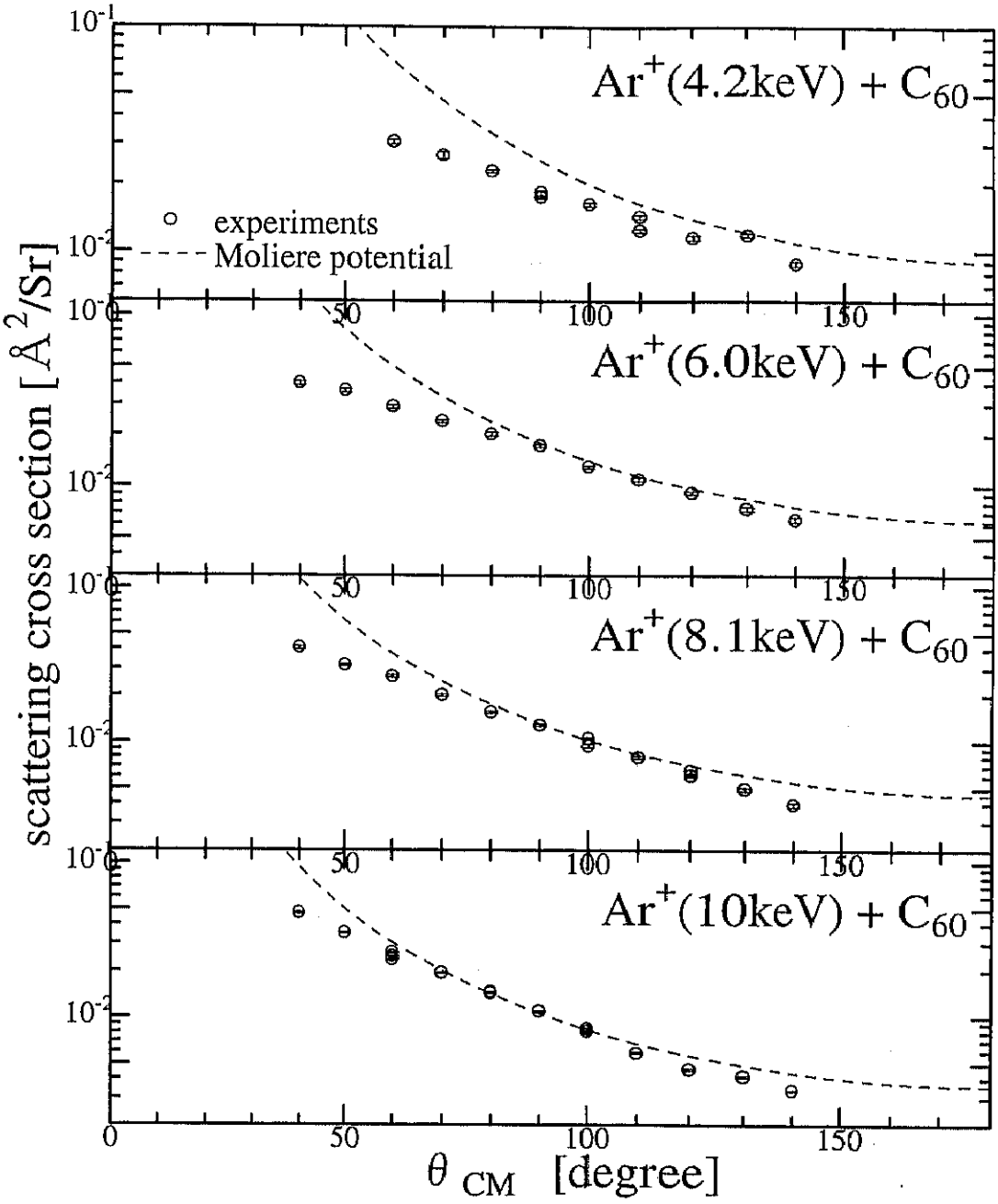

Figure 28: The differential cross sections of collision argon atom with carbon in C_{60} target at 4225eV to 10keV: The discrepancies become small as increasing the collision energy.

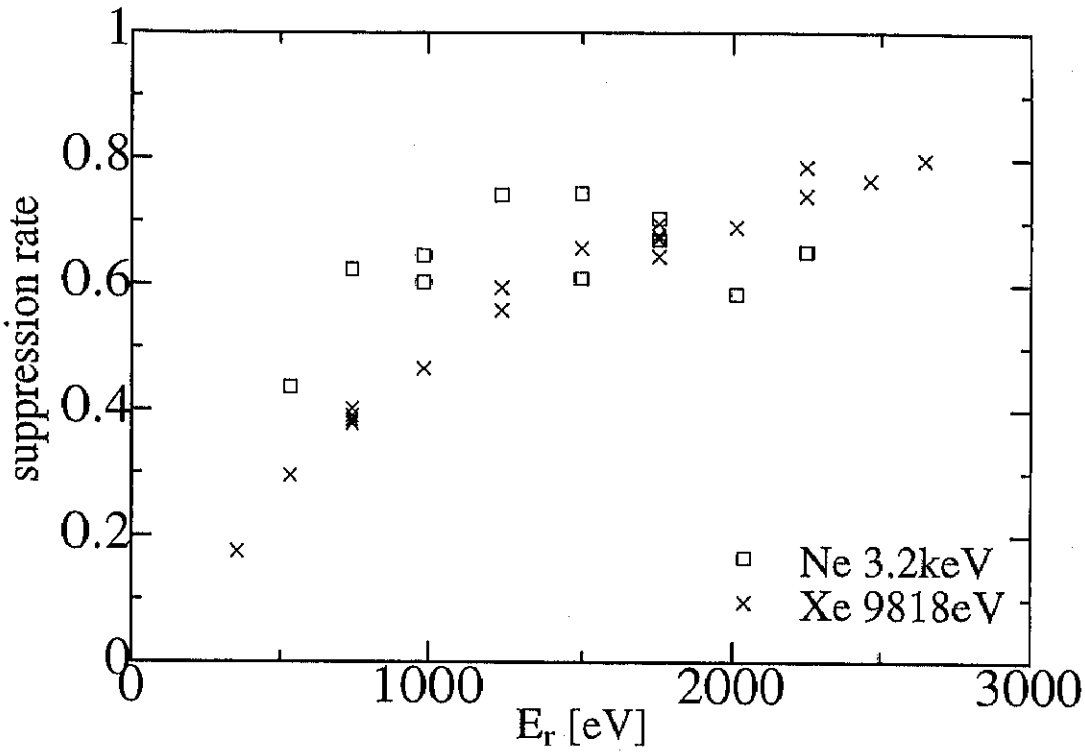

Figure 29: The suppression rate dividing measurement value by the calculation as the function of recoil energy of carbon deduced from TOF measurements: These different trends of suppression show that the suppression is not only explained the multi-collision of carbon atom in C_{60} because its trend is independent on the recoil energy.

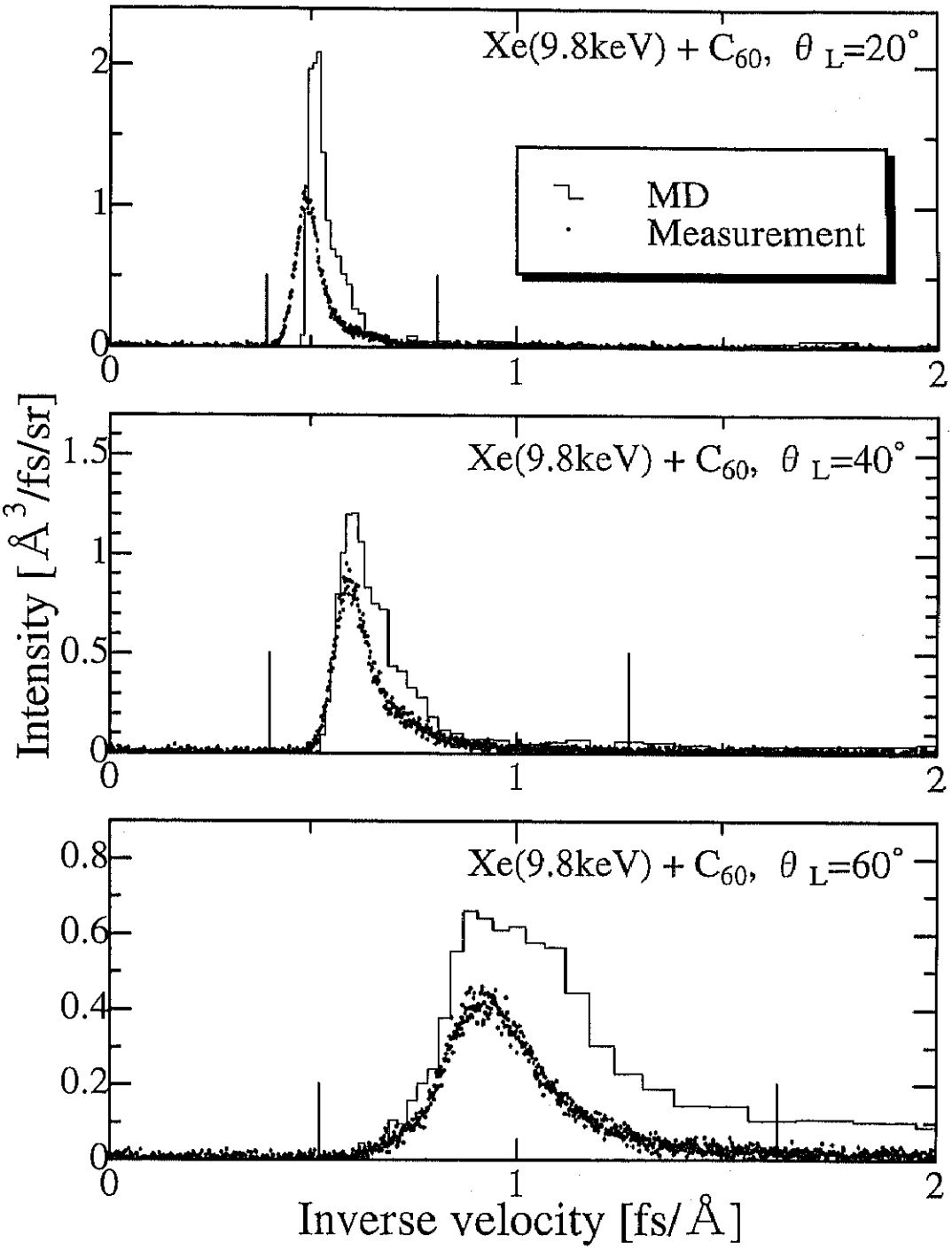

Figure 30: TOF spectra of recoiled carbon atoms in each angles from bombardment of C_{60} by Xe beam at 9818eV, which are measurements and Molecular Dynamics simulations: The perpendicular bars indicate the area of integration for counting yield in each spectrum.

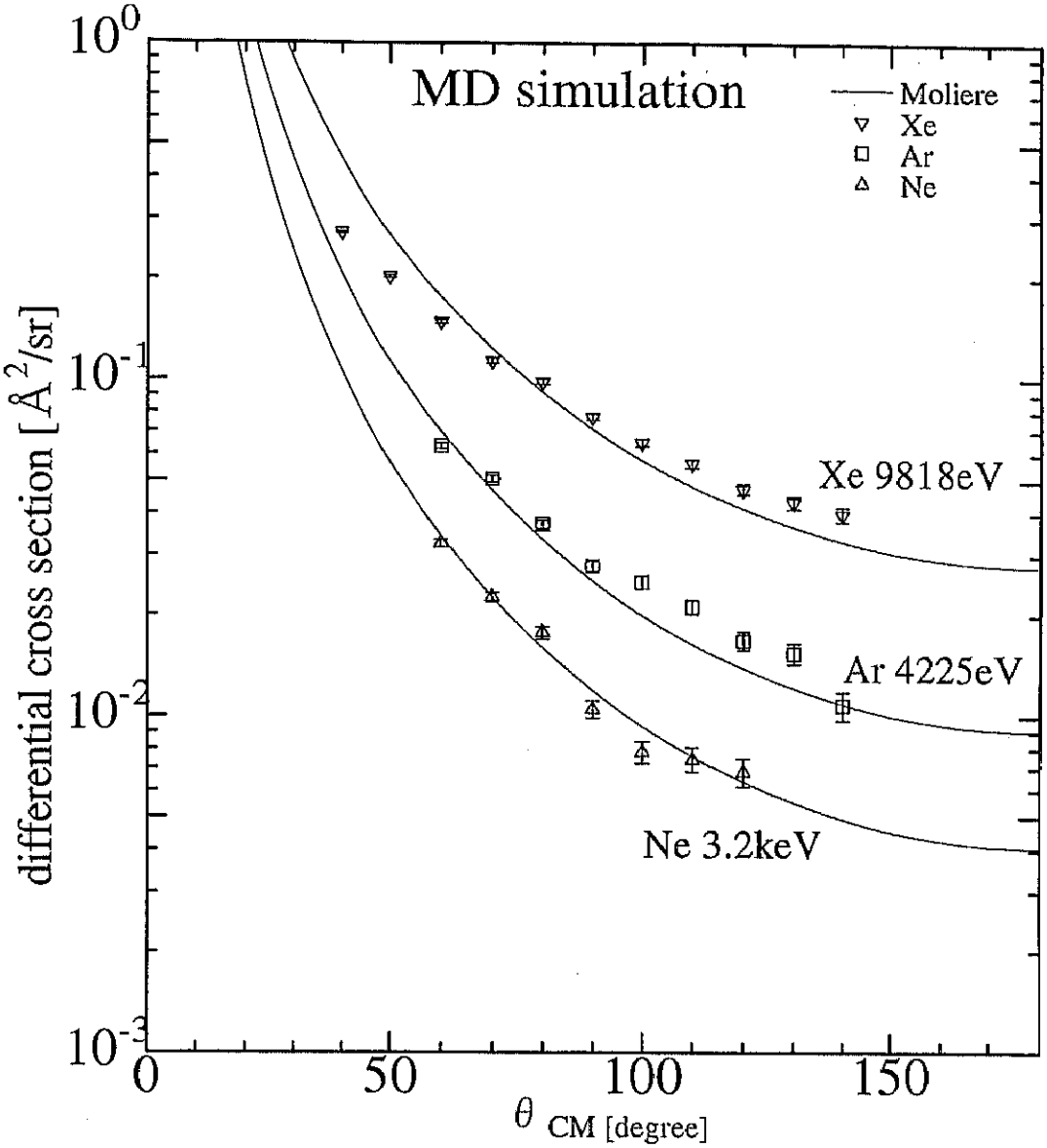

Figure 31: The differential cross sections deduced by theoretical calculation of molecular dynamics simulation: The results of Ne and Ar indicate there are no special things unlike the experimental results. In Xe case, it seems that the results are a little different from binary calculations, due to the many body collision at the same time.

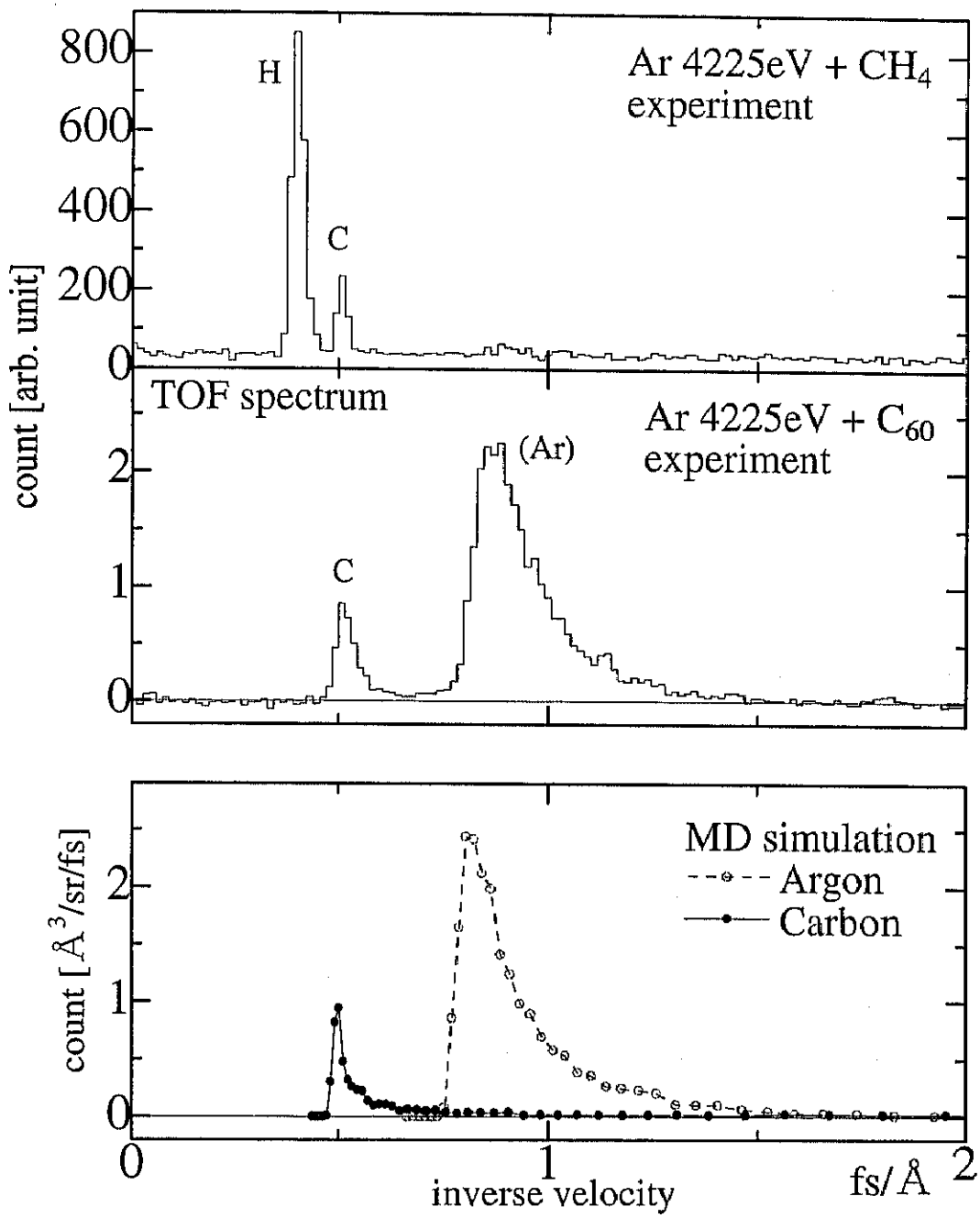

Figure 32: The inverse velocity spectra of the measurements for CH_4 and C_{60} target and the result of Molecular Dynamics simulation: The big peak shown in the figure of Ar + C_{60} which is never shown in Ar + CH_4 is estimated the scattering Ar by the results of MD simulation.

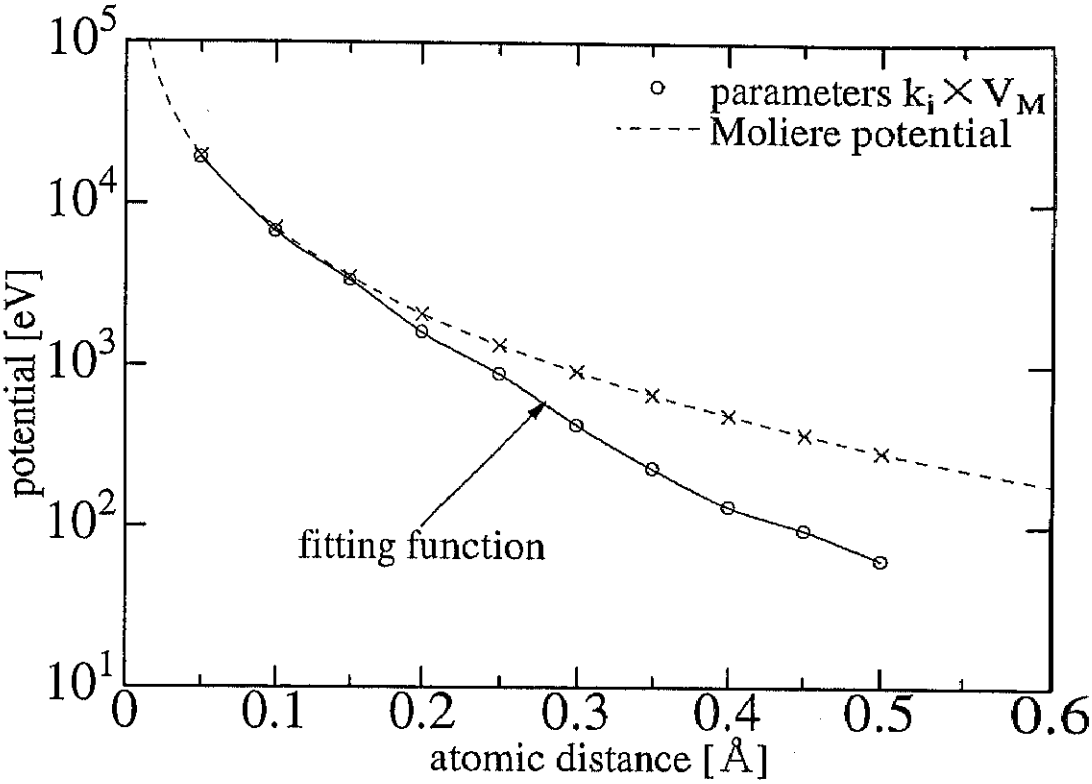

Figure 33: The function of free parameter optimization: × symbols indicate initial value for the optimized parameter search. The least square fitting was done between differential cross section calculated using the fitting function and measurements.

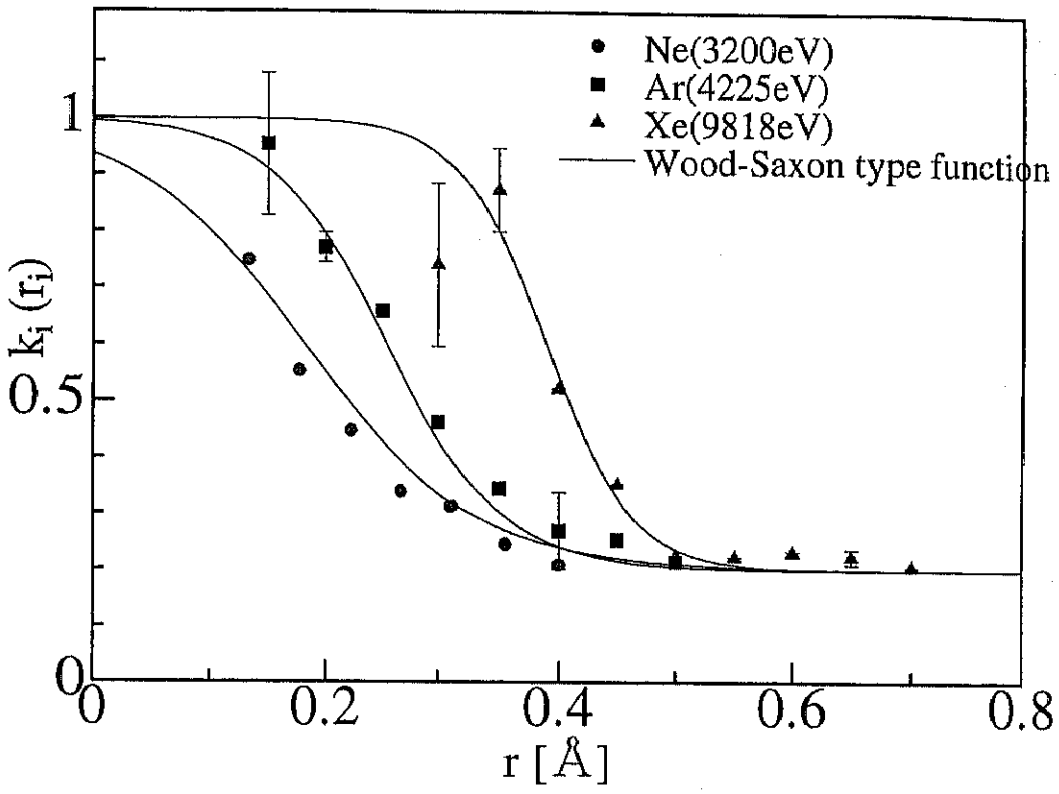

Figure 34: The results of free parameter optimization and speculations of the additional screening function as the Woods-Saxon type functions:

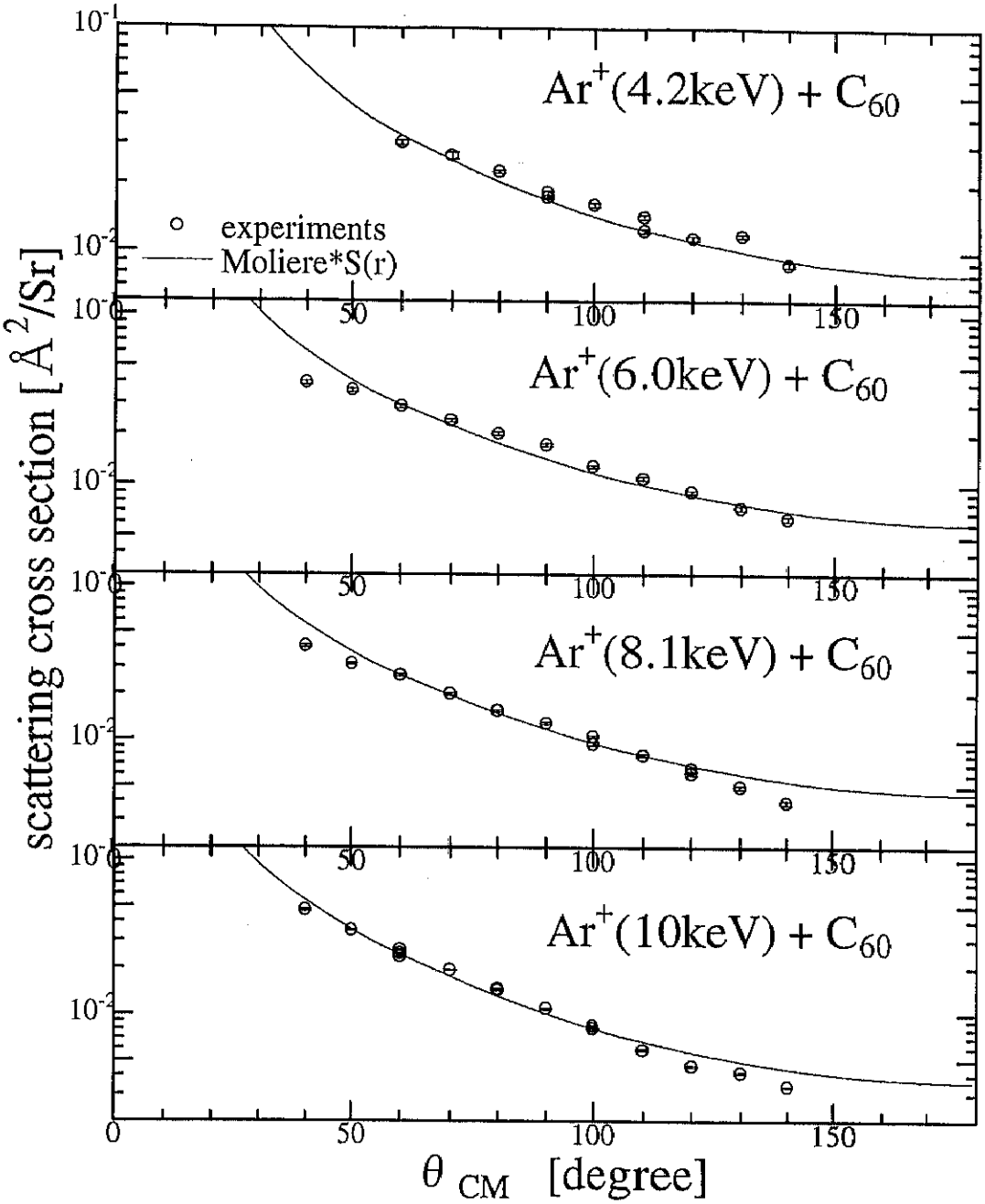

Figure 35: The result of fitting to $Ar^+ + C_{60}$ experiments at several energies:

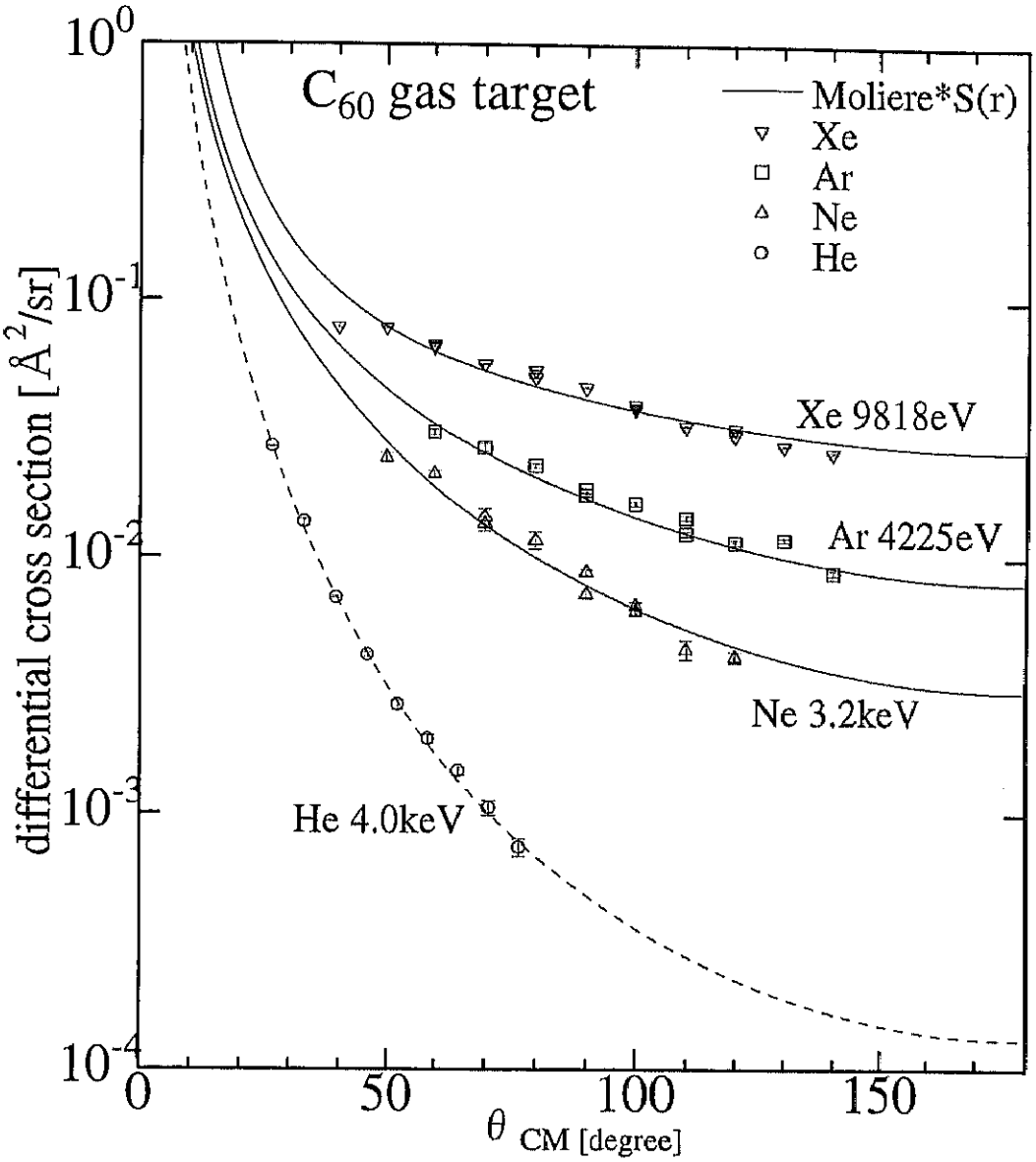

Figure 36: The results of fitting to Ne^+ and $Xe^+ + C_{60}$ experiments.

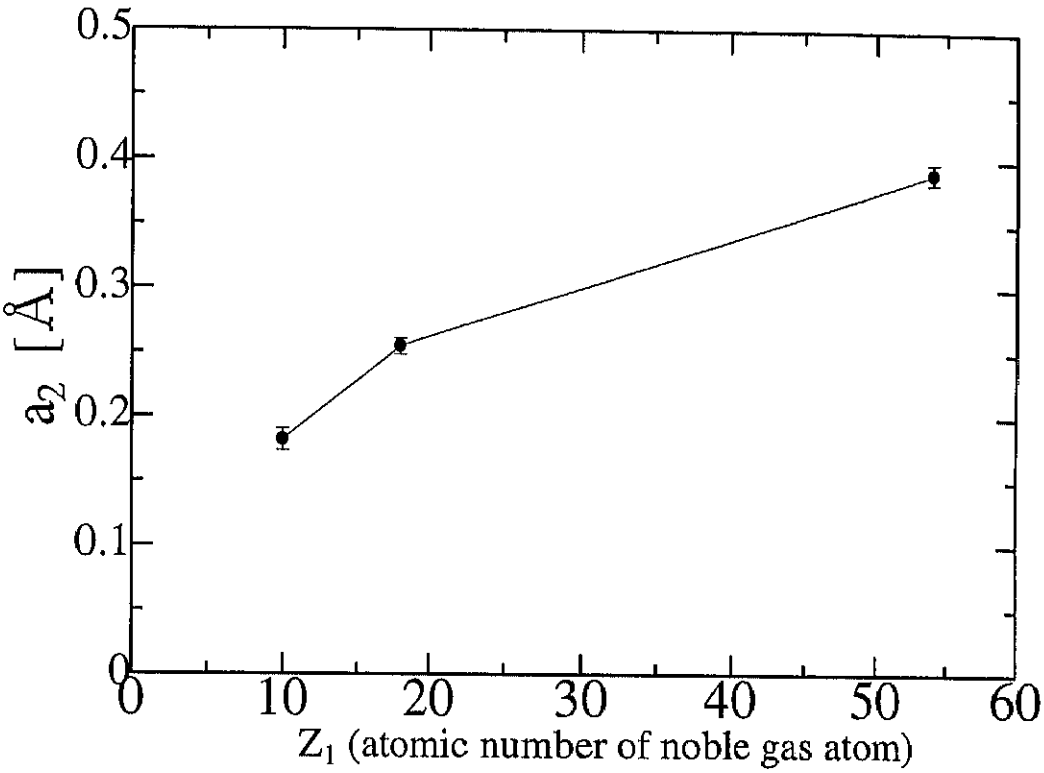

Figure 37: Z_1 dependence of the parameter a_2:

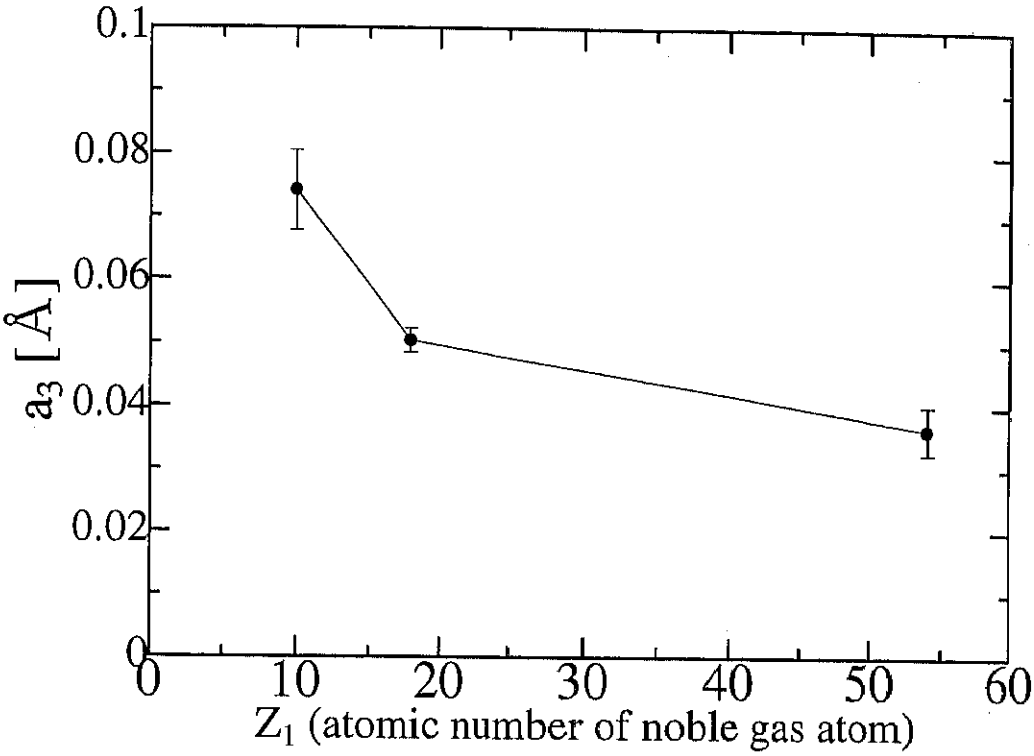

Figure 38: Z_1 dependence of the parameter a_3:

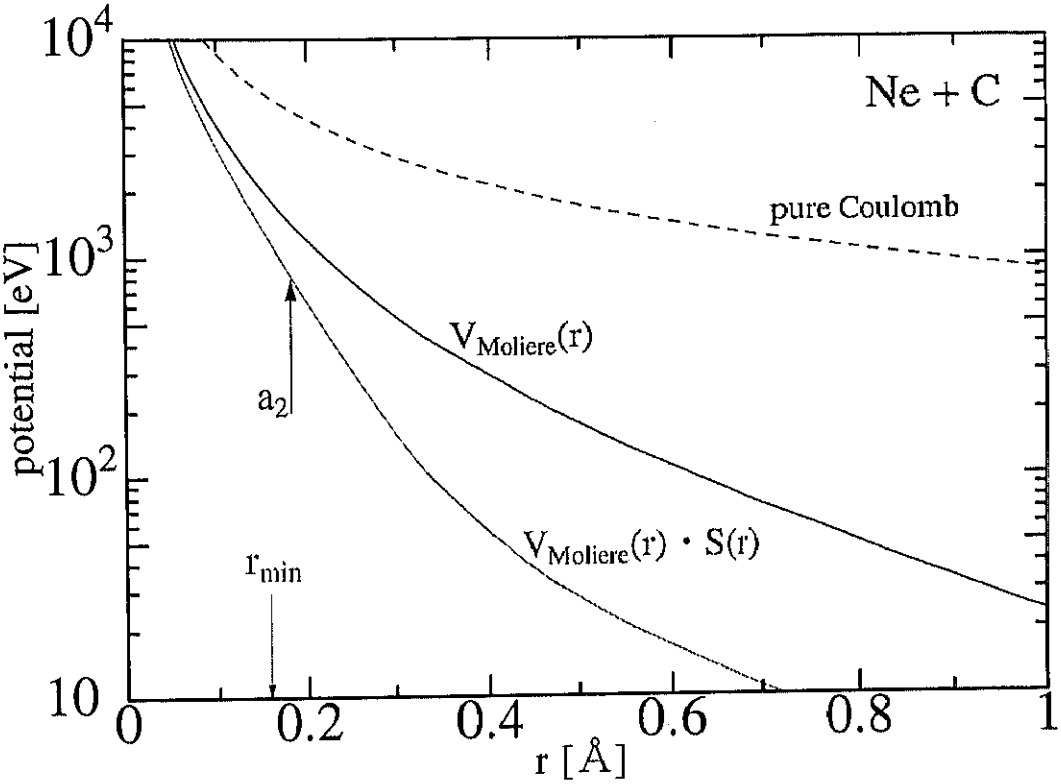

Figure 39: Interatomic potentials of pure Coulomb, Molière and new interatomic potential, $V_M(r) \cdot S(r)$, for Ne + C: The r_{min} indicates the distance of closest approach in present experiment.

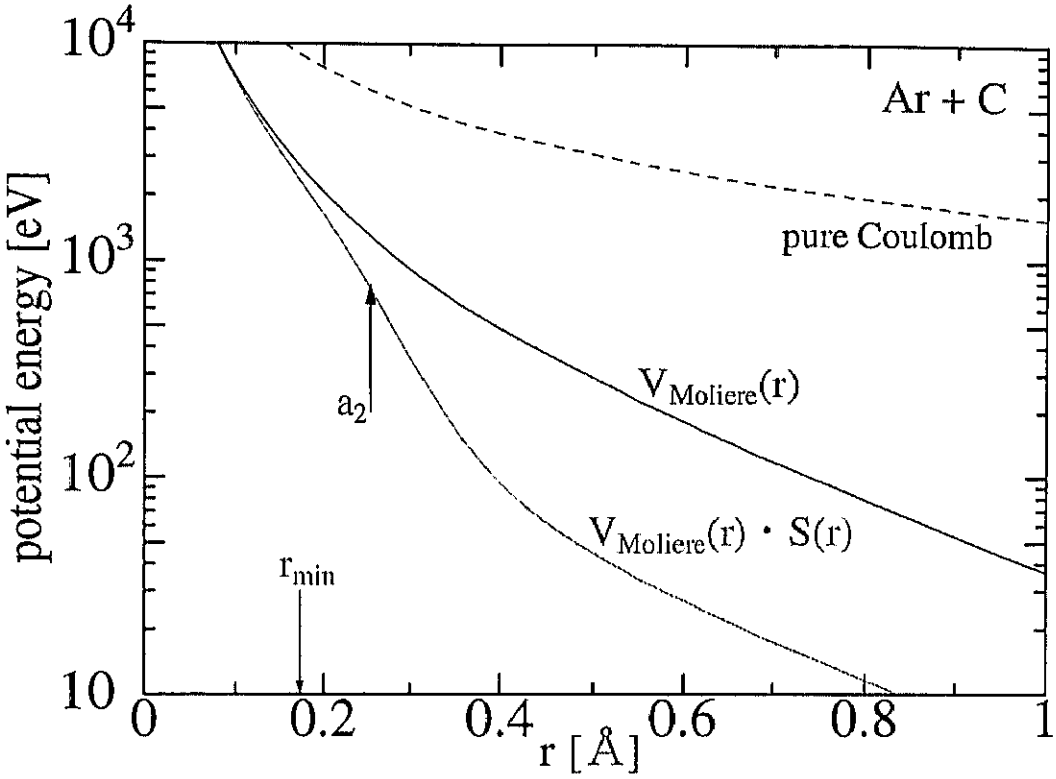

Figure 40: Interatomic potentials of pure Coulomb, Molière and new interatomic potential, $V_M(r) \cdot S(r)$, for Ar + C: The r_{min} indicates the distance of closest approach in present experiment.

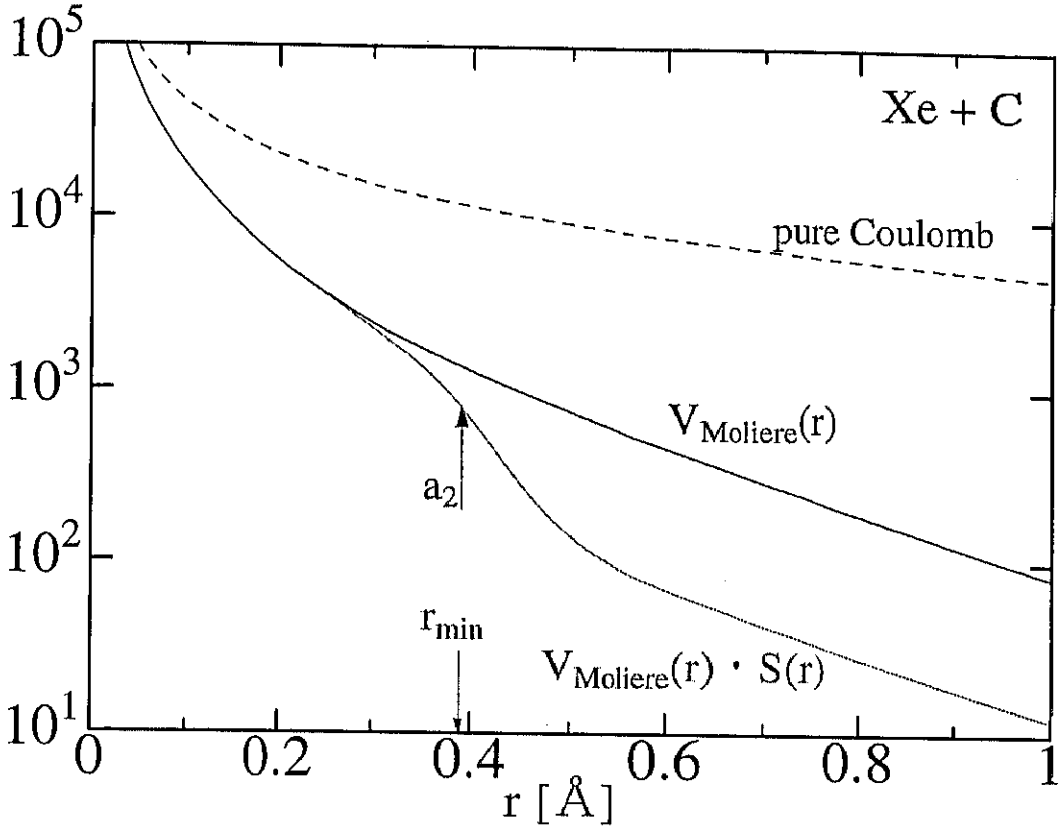

Figure 41: Interatomic potentials of pure Coulomb, Molière and new interatomic potential, $V_M(r) \cdot S(r)$, for Xe + C: The r_{min} indicates the distance of closest approach in present experiment.

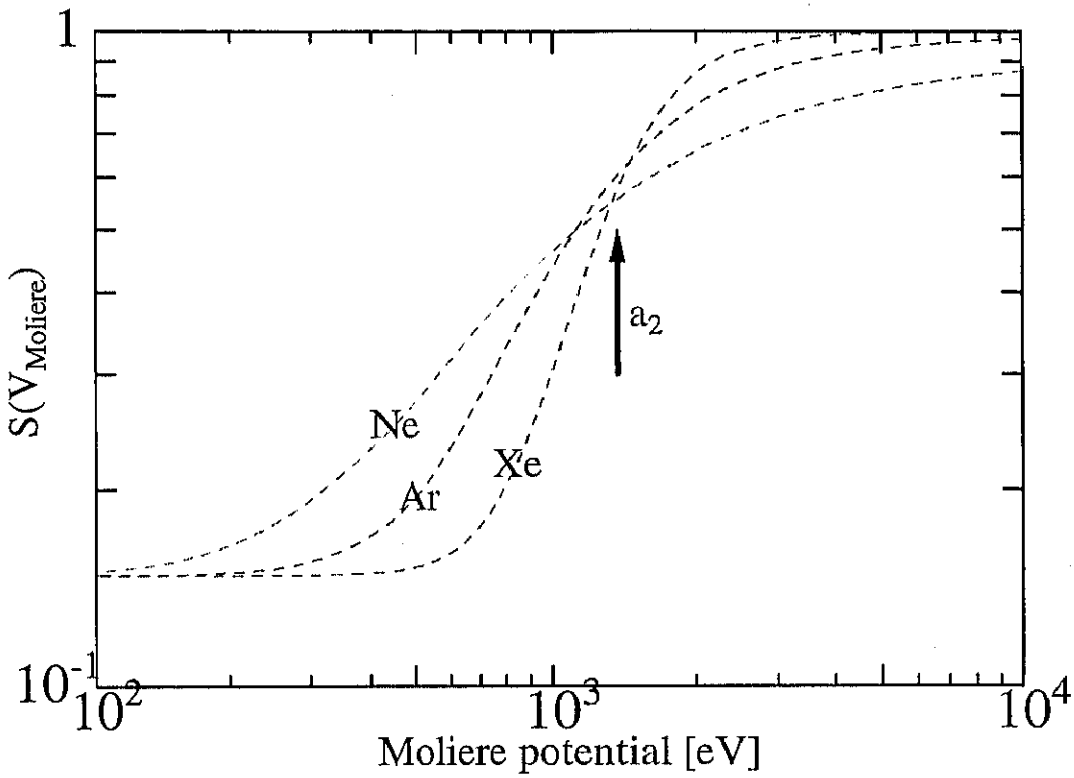

Figure 42: Additional screening function scaled by Molière potential: The additional screening functions scaled by binary potential well agree with each other in spite of difference of incident atomic number. This fact is very interest and probably suggests some unknown physical mechanisms.

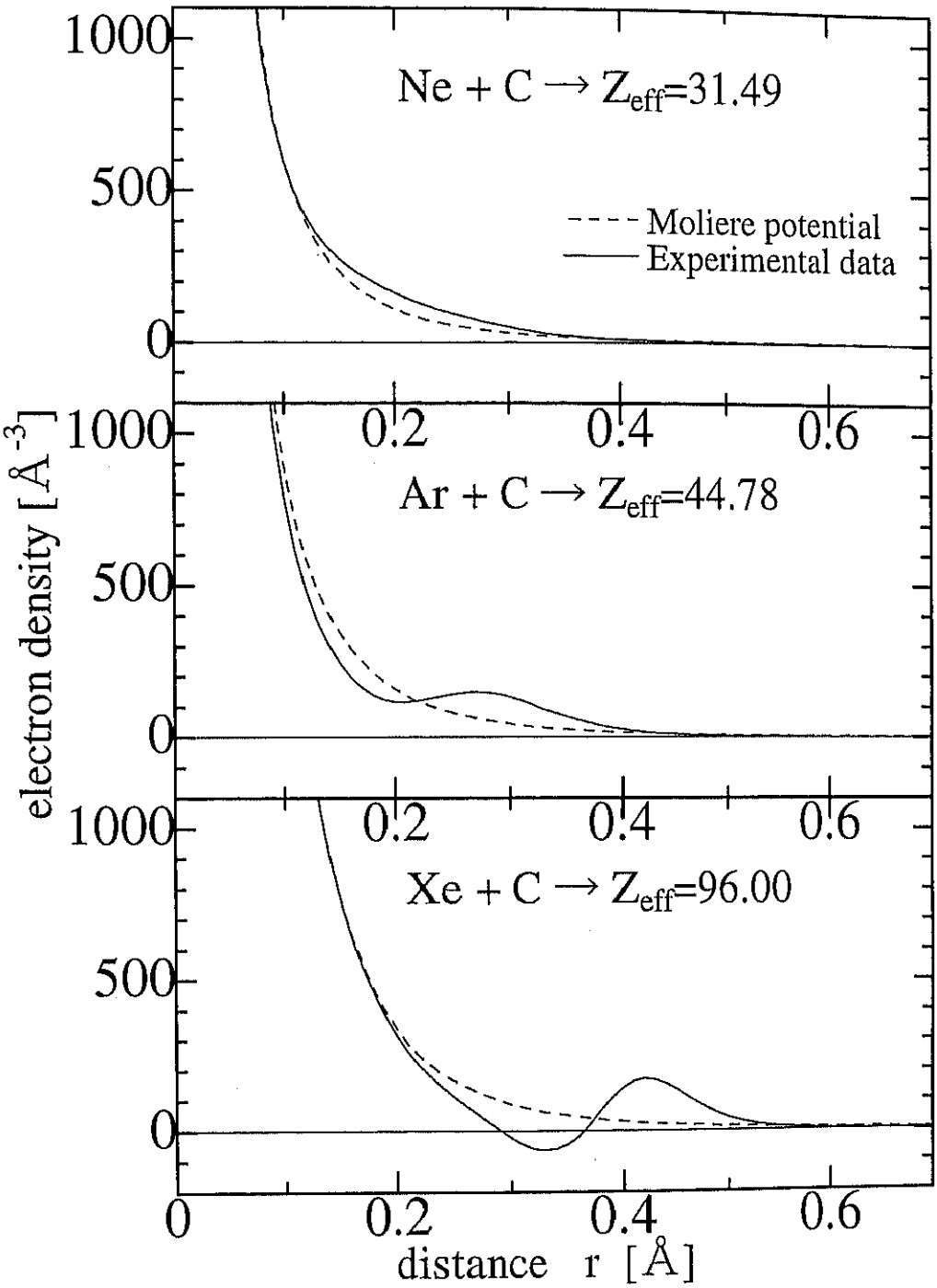

Figure 43: The electron density distribution of reduced charge Z_{eff}, which calculated using interatomic potential by Poisson's equation:

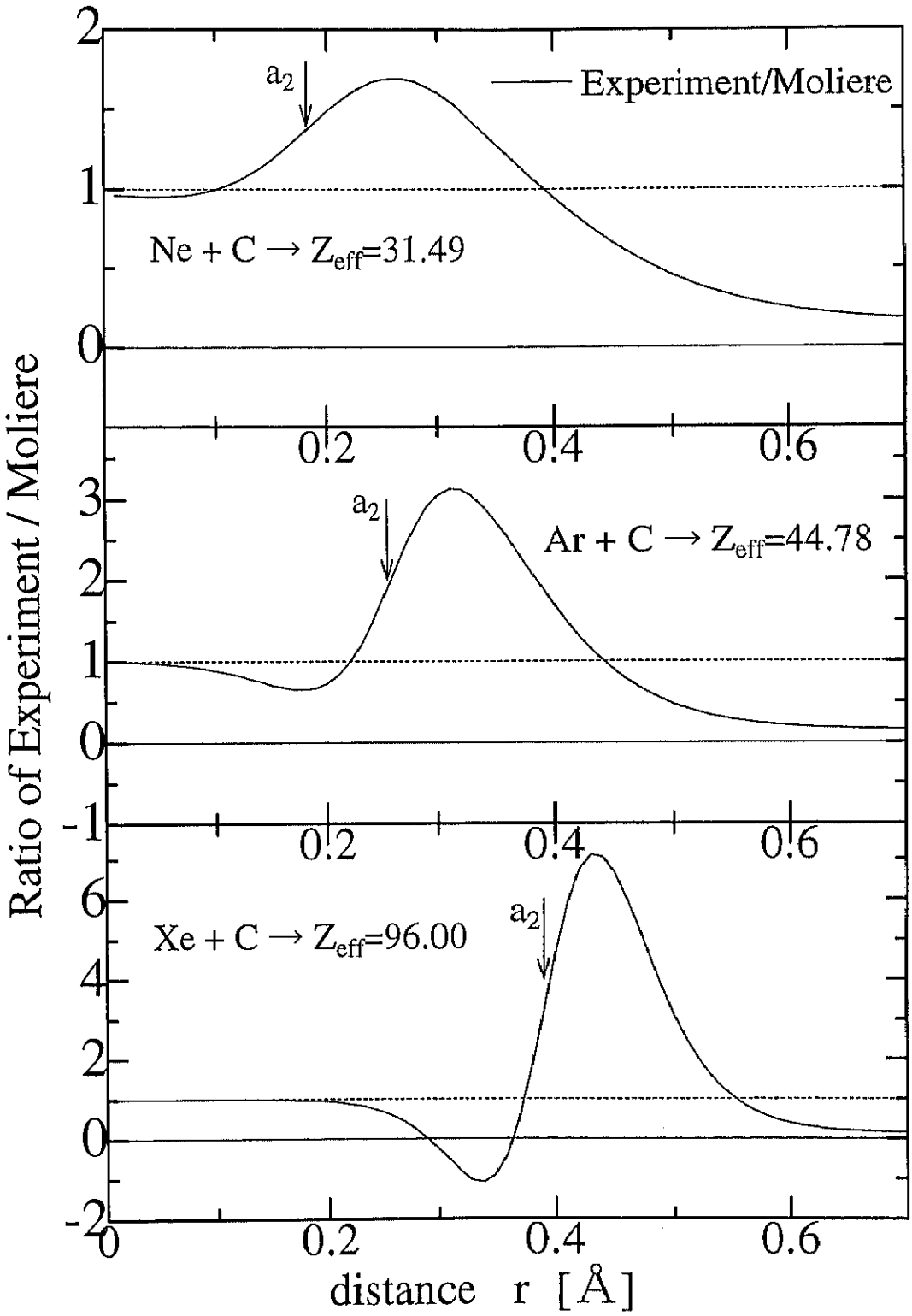

Figure 44: The ratio of the experimental electron density to the Molière density:

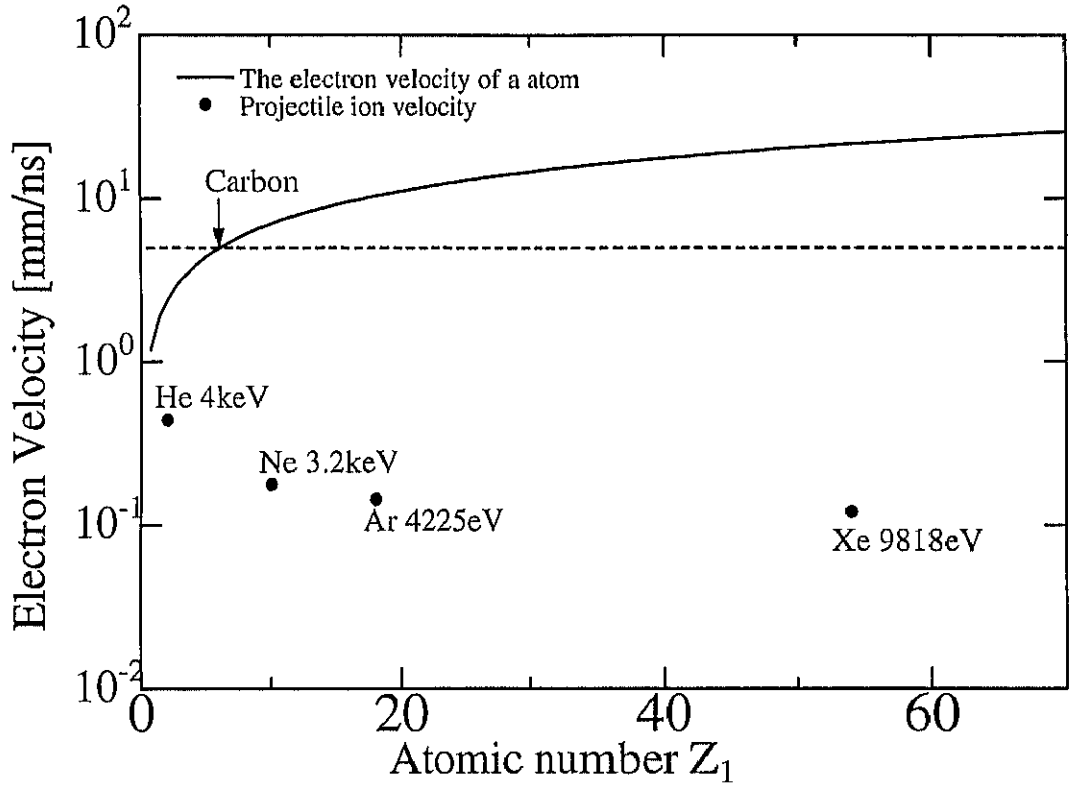

Figure 45: The average electron velocity in an atom deduced by Thomas-Fermi model: The motions of incident ions are much smaller than the average value of electron velocity in each atom and C_{60}.